Study of $K\alpha$ absorption structures in a subcritical-density laser-produced plasma

C. A. Back, C. Chenais-Popovics, P. Renaudin, J. P. Geindre, P. Audebert, and J. C. Gauthier
Ecole Polytechnique, Laboratoire de Physique des Milieux Ionisés, 91128 Palaiseau CEDEX, France
(Received 24 February 1992)

The study of $K\alpha$ line absorption by point-projection backlighting is presented for a laser-produced aluminum plasma at electronic densities below 5×10^{21} cm^{-3}. The appearance of ionic species as a function of distance from the target is measured absolutely by the use of a knife edge as a spatial fiducial. These data are used to determine the gradient of the average charge as a function of space. A non-local-thermodynamic-equilibrium ionization model has been developed to determine temperature and densities consistent with this measure. Comparisons with hydrodynamic codes are presented, along with a discussion of the inferred temperature.

PACS number(s): 52.25.Nr, 52.70.La, 52.40.Nk, 32.30.Rj

I. INTRODUCTION

$K\alpha$ absorption spectroscopy has proved to be an extremely useful tool to probe the ground-state populations and ionization balance of a dense plasma [1–5]. It relies on the absorption of photons from an external source, the backlight, by the $1s$-to-$2p$ transitions of ions having a vacancy in the $n=2$ shell, i.e., the F-like to the He-like species. The absorption in general involves several transitions but tends to manifest well-separated structures, each localized in a narrow spectral range which can be attributed to a particular ion. The absorption structure of a highly ionized atoms is located at lower wavelengths than that of a lesser ionized atom of the same species because its electronic screening is lower. These characteristics permit the quantification of the separate ionic species and are some of the reasons why absorption studies are so useful in characterizing nonemitting plasmas.

Traditionally, the $K\alpha$ lines have been used to determine opacity or infer temperature of a dense tracer layer. However, in this paper we show that by measuring the absorption in a direction perpendicular to the expansion, it can also be applied to map out the ionization distribution in the plume of a laser-produced plasma. These experiments measure the average Z as a function of distance from the surface of the target for a subcritical density plasma. In particular, the onset of the He-like species is determined by detecting the presence of lesser ionized atoms and their absolute locations from the surface of the target. In addition, this paper includes an inference of temperature, based on the hydrodynamic calculations of the density at the time the plasma was probed.

This study of the ionization balance is particularly relevant to photopumping studies and x-ray recombination lasing schemes because it characterizes the plasms at precisely the time of interest. Spatial distribution measurements can begin to address unresolved issues in photopumping such as the location and spatial extent of fluorescence [6]. Or for lasing studies, an ionic species of interest, such as Li-like, can be quantified and spatially correlated with the gain.

II. EXPERIMENTAL SETUP

In this experiment, a plastic foil having an aluminum microdot of 270 μm diam embedded in a plastic foil was irradiated to create a cold He-like aluminum plasma which was then backlit by a bright photon source. The plasma was created by one beam of the Nd:glass LULI laser with a pulse duration of 500 ps, a wavelength of 0.53 μm, and a flux in the range of 10^{12}–10^{13} W/cm^2. This laser intensity was chosen to create a predominantly He-like ion plasma. The focal spot containing approximately 80% of the laser energy was 360 μm diam so that the microdot was overfilled, producing a surrounding plastic plasma which partially tamped the lateral expansion of the aluminum plasma, thus reducing the lateral gradients in the plasma. Also a random-phase plate was used to produce a more homogeneous laser irradiation [7].

A second laser beam at 0.26 μm and 500 ps was tightly focused on the end of a fiber coated with samarium to generate a backlight for point-projection spectroscopy [8–10]. The target and fiber were aligned to ensure that the $3d$-$4f$ emission from the backlight plasma passed through the aluminum plasma, in a direction perpendicular to the blowoff, and was recorded by a time-integrating crystal spectrometer. The backlight probe was delayed 1.4 ns after the peak of the laser beam that created the plasma.

To obtain high resolution, the source size of the backlight was minimized by the following technique. The laser beam was focused to 80 μm diam on the end of a fiber that was aligned such that the flat face of the cut was parallel to the line of sight of the spectrograph. In this geometry, the source extension is equivalent to the length of the 2-keV emission region from the surface of the fiber face. Previous measurements by the method of penumbral imaging indicate that the source size is on the order of 10 μm [11]. The backlight x-ray emission follows the pulse of the laser, and its duration, measured by time-resolved spectroscopy, is 500 ps.

The experimental setup, shown in Figs. 1 and 2, depends on two components, a crystal spectrometer and a

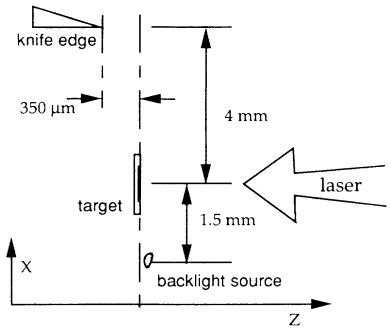

FIG. 1. Closeup of the experimental arrangement. The line of sight of the spectrograph defines the axis of the system for the alignment of the target surface and backlight source and is parallel to the x axis. The positive z axis is the direction of the plasma expansion.

knife edge. The crystal spectrometer employs an ammonium dihydrogen phosphate crystal (ADP, $2d=10.64$ Å) to record the time-integrated transmission spectrum of the backlight. The knife edge serves two main purposes: (1) its shadow cast by the backlight, provides a region of the film where the self-emission can be directly recorded, and (2) the edge of its shadow provides a spatial fiducial. From the edge position and the magnification of the system, the absolute position of the original surface of the target is obtained.

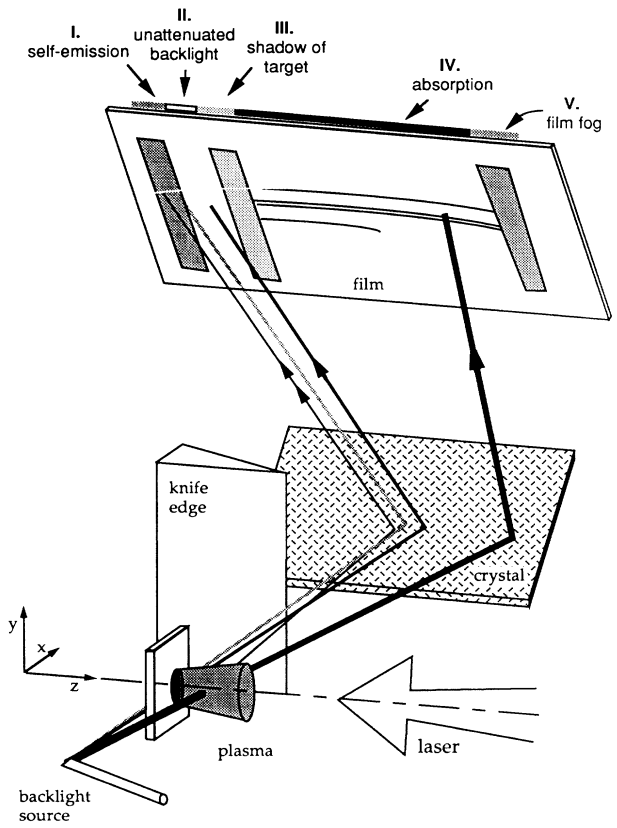

FIG. 2. Schematic diagram of the experimental arrangement and the film regions. The line with the double arrow head shows the path of the photons due to self-emission onto the region which is shielded from the backlight by the knife edge. The dark solid line shows the backlight photons that probe the plasma. The grey line shows the projection of the knife edge onto the film by the backlight.

The spectrograph was positioned so that its line of sight was perpendicular to the plasma's principal axis of expansion, the z axis in Fig. 1. This side-on geometry, coupled with the use of the microdot, defines the length of plasma that is probed. The absorption lengths vary from 270 to 200 μm due to the changing path length of the Bragg-dispersed backlight photons of wavelengths 8.3–7.7 Å through the column of plasma. The length of plasma probed is thus defined which enables a determination of the ionic density from the absorption spectra.

Precision alignment to the spectrograph's line of sight is essential to the analysis and involves three steps for each shot. First, the target is rotated so that its surface is parallel to the line of sight of the spectrograph. Second, the knife edge was placed 4 mm from the plasma and was offset by 350 μm from the line of sight. This offset allows the backlight to be recorded unattenuated by passing between the unirradiated surface of the target and the knife edge. Third, the backlight fiber is aligned by the technique described above to minimize its source size. The distance from the plasma to the backlight source was 1.5 mm, which gives a magnification factor of 80. The target, spectrometer, backlight, and knife edge were aligned on a plaque outside of the vacuum chamber using microscope objectives, and then placed inside the chamber on a kinematic mount.

III. EXPERIMENTAL RESULTS

A. Qualitative discussion of data

Five regions of data can be identified on the film and are essential to the proper analysis of the spectrum as a function of space. Figure 2 shows a schematic of the experimental setup and the paths of the photons from the backlight and the plasma onto the film to illustrate the difference between these regions. Region I is the time-integrated self-emission directly from the plasma. Since the self-emission is not spatially or temporally resolved it must be subtracted from the rest of the data in order to determine the true absorption data. The right border is the spatial fiducial produced by the knife edge. Next in region II, the unattenuated backlight spectrum and the self-emission are recorded. Following this is region III, the shadow of the target created by the backlight. Region IV, the absorption region, records both the backlight photons which pass through the plasma as well as the self-emission. The fine dark lines are the absorption features of different ionic species and are labeled in Fig. 3 by their isoelectronic sequence name. Finally, region V is the film fog which must be subtracted from all the data before the conversion from density to intensity is performed. Figure 3 presents two representative photos of the data that are obtained at laser energies of 3 and 5 J which bracket the appearance of the emission of the He-like resonance line. The plasma is probed 1.4 ns after its

creation in both cases, but the extension of the $K\alpha$ absorption lines for the Li-like or lower ionic stages in these photographs is markedly different for the factor 2 change in energy.

Analysis of the digitized data provides the intensity traces as a function of position from the surface of the target. For each shot, the curvature of the spectral lines due to the point source backlight is corrected and the data are then processed by the following steps: (1) the film fog is subtracted, (2) the film density is converted to intensity, (3) the intensity of the self-emission of the plasma is subtracted, and (4) the spectrum at each position is divided through by the unattenuated backlight spectrum. The original surface target position corresponds to zero on the x axis, and the plasma expands in the positive direction. The spectra were space averaged along the target normal over steps of 2 or 1 mm on the film, which corresponds to 25 or 12.5 μm, respectively, at the source.

The traces in Fig. 4 are for the photograph shown in Fig. 3(a), in which the self-emission of the He-like Al, $1\,^1S_0-2\,^1P_1$ resonance line emission is absent. Close to the target, the ion species F-like through Be-like are identifiable. This region corresponds to the thermal front where the gradients in temperature and density change quite rapidly as a function of distance, and several ionic species appear. The data show that in a region 30–60 μm from the target surface, O-like through Li-like ions exist during the 500-ps duration of the probe. At about 100 μm the He-like ion is the strongest ion in absorption and this trend continues to the maximum distance probed.

B. Measurement of average Z

The ionic balance of the plasma can be represented by the average ionic charge, $\langle Z \rangle$, which can be expressed as follows:

$$\langle Z \rangle = \frac{\sum_i Z_i n_i}{\sum_i n_i} ,$$

where the sum of the charge Z_i and the total ionic population n_i are over the ionic species i that exists in the plasma. The population densities can be determined by matching the experimental absorption spectra with the calculated absorption spectra and then they can be plugged directly into the equation shown above to yield the average charge Z. These populations are difficult to measure well because they depend on the absolute number of photons absorbed by the plasma and require absolute calibration of the diagnostic.

However, the above equation can be rewritten as a sum over the ionic fractions $\langle Z \rangle = \sum_i Z_i f_i$. Since each ion gives rise to a characteristic structure and each ionic species can be spectrally resolved, this allows us to normalize out the fluctuations depending on absolute numbers by considering the ensemble of ionic species. In short, the change in the relative strengths of the absorption features directly reveals the behavior of the ionization balance as a function of space.

In this paper, a comparison between the experimental spectrum and a synthetic spectrum that has been con-

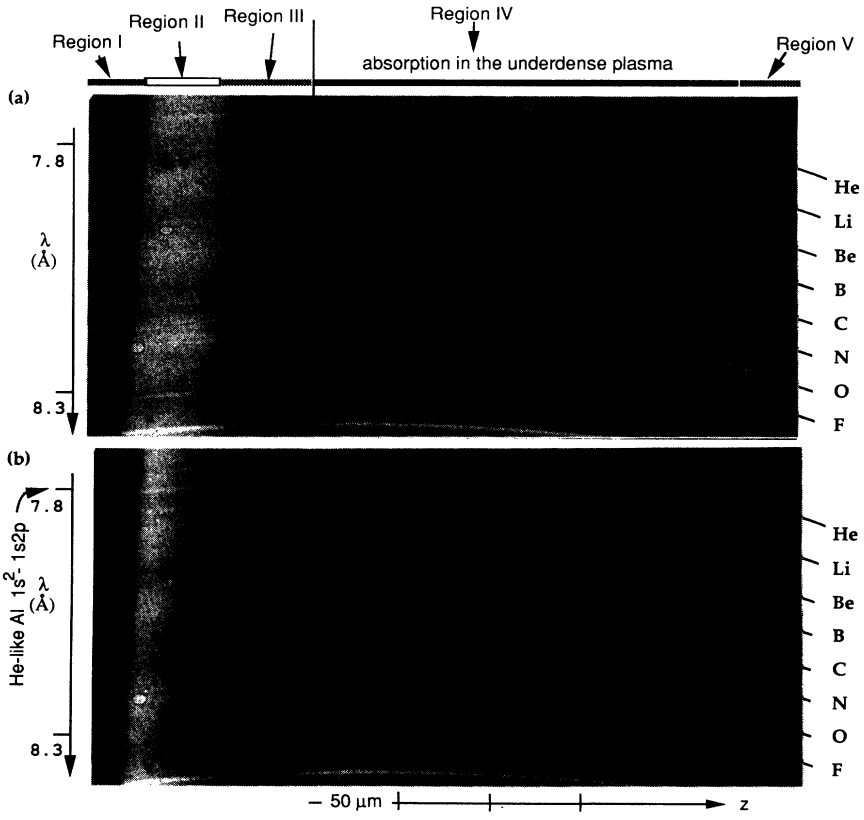

FIG. 3. Two photographs of the data. The film regions are identified in the upper margin. The dark lines correspond to absorption and are labeled by their isoelectronic sequence, i.e., Al XII=He. The absorption for a plasma created by a 0.53-μm laser: (a) laser energy 3 J, no He-like resonance line emission is visible; (b) laser energy 5 J, the He-like Al, $1\,^1S_0-2\,^1P_1$, resonance line in emission is indicated in region I.

volved with an instrumental width is performed to determine the experimental average charge. The mechanics of generating a synthetic spectrum using a calculated local-thermodynamic-equilibrium (LTE) ionization balance are described in a previous paper [3]. In contrast, to generate these spectra the calculated ionization balance is replaced by a user input ionization balance in the modeling. The species of ions used in the input are those which appear in the data plus the neonlike, hydrogenlike, and fully stripped ions. The theoretical ionic fractions, and thus the average ionic charge, are modified in an iteration process until the synthetic spectrum matches that observed in the experiment. Examples of the fits are shown in Fig. 4(b).

Figure 5 shows the reduced data for the two shots shown in the photographs. The average charge of the plasma rises sharply with the onset of the ionic species having an open L shell. For these intensities, the appearance of the O-like through He-like ions occurs within an ~ 35-μm region. In particular, the traces at 37.5 and 62.5 μm in Fig. 4, photograph 3(a), show that several ionization stages are present, as expected, since it reflects the

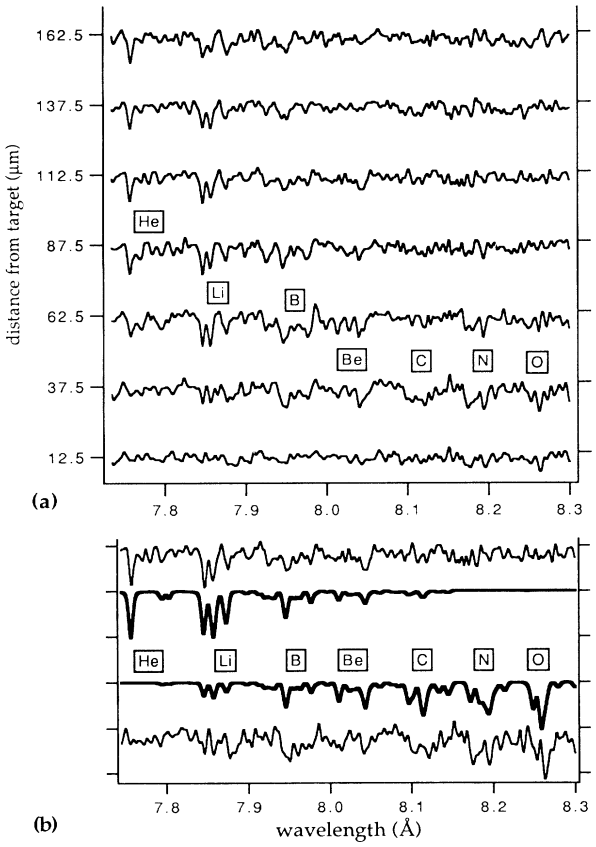

FIG. 4. Transmission spectra corresponding to photograph 3(a). In (a) the experimental spectra, taken at steps 25 μm apart, show the extension of the absorption structures as a function of space. The intensity of each spectrum is in arbitrary units. In (b) the experimental spectra are presented with the synthetic spectra (bold lines) that are used to determine the average ionic charge. The upper spectrum is taken at 25 μm and the lower spectrum at 112 μm from the target surface.

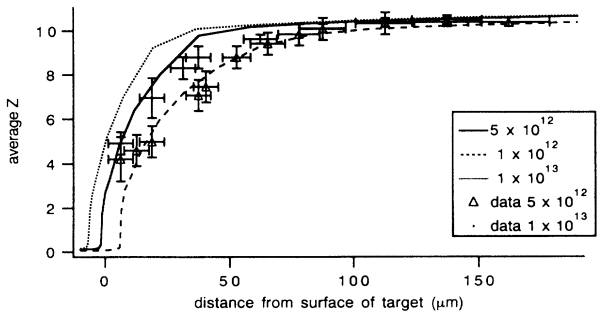

FIG. 5. Average Z as a function of distance from the target surface. The experimental laser fluxes were in the range of 5×10^{12} to 1×10^{13} W/cm^2. Hydrodynamic code predictions of average charge $\langle Z \rangle$ are shown for three different fluxes.

relaxation of the ablation front after the laser pulse. Once the He-like state is reached, it persists for a large distance because the laser intensity is suited to create a predominantly He-like ion species and does not overionize to the H-like species.

Since the measurement shown here is taken at late times, one might expect that the plasma will significantly recombine, however it does not. The time-integrated He-like resonance line self-emission is extremely weak for these two shots, which indicates that the plasma is never ionized enough to create a strongly emitting H-like plasma. Therefore, the plateau at $\langle Z \rangle = 10.4$, which extends out for a long distance, indicates that the bulk of the plasma has not significantly recombined even at this late time because of the falling density at large distances from the target surface.

If we estimate the velocity of the bulk of He-like plasma by its position of maximum appearance, 100 μm, divided by the time of travel, 1.4 ns, we find that the velocity is on the order of 7×10^6 cm/sec, which is roughly the velocity in the thermal front when it is created. The absorption for the He-like ions in shot 3(b) peaks at about half this distance, therefore implying a velocity of approximately half this value. This decrease in velocity occurs with increasing laser energy and will be further examined in the next section with the use of the codes.

The error bars in the average charge are due to the sensitivity of the fitting method and are shown in Fig. 5. However the spatial resolution is due to a combination of the error introduced by the technical limits of the source size, 10 μm for all points, and by the temporal smearing caused by the 500-ps duration of the backlight. Over the range shown, it varies from 10 to 77 μm. Two physical effects contribute to the spatial smearing during the 500-ps duration: first, the ions recombine as the plasma cools, which may change the bulk distribution of ions available for the absorption, and second the plasma moves in space.

The first effect is estimated by examining the ionization balance calculated by the simulations. Although the recombination is not experimentally differentiable from the expansion, the codes show that the volume of plasma

that has a dominant fraction of He-like ions at the peak of the pulse still has the dominant fraction 1.4 ns later. Calculations show that an average Z time integrated over 500 ps is virtually identical to the average Z predicted by the code at a given instant in the middle of the time frame. This indicates that the plasma does not recombine enough during the backlight to change the distribution. Therefore, recombination does not make a significant contribution to the error.

For the second effect, plasma expansion during 500 ps, a differential smear factor must be taken into account which is dependent on the velocity. The velocity distribution calculated by the code FILM at the experimental probe time varies from 5×10^5 to 1.5×10^7 cm/sec along the average Z gradient that spans the F-like to He-like ions. The horizontal error bars in Fig. 5 include these contributions when they dominate the spatial resolution due to the point source size.

Although a shorter backlight is necessary for better resolution, the velocity, and thus the smearing, is small for the region where the thermal gradient exists. Therefore, the spatial distribution found in these experiments will not qualitatively change if a shorter backlight is used.

IV. HYDRODYNAMIC SIMULATIONS

Hydrodynamic simulations were performed in 1 and 1.5 dimensions using the Langrangian hydrodynamics code FILM. In this simulation, the laser energy is deposited by inverse bremsstrahlung and the electron conduction is modeled by a delocalized flux model [12], or the classical Spitzer [13] with a flux limiter.

In Fig. 5, the simulations using a flux limiter of 0.12 are shown for different incident laser intensities. The front can be characterized by its absolute position and its slope. When the laser intensity is varied, the gradient of the average Z tends to have the same slope, but is displaced relative to the target surface. At higher intensities, the foot of the ionization gradient is closer to the original surface of the target, which indicates that the absolute positions of the average Z in space depend on the penetration of the ablation front. The slope does not significantly change as a function of time, thus the late time behavior is dominated by the hydrodynamic expansion of the initial ionization in the dense plasma. Physically, the thermal front of interest occurs in a more embedded denser region as the intensity is increased. Therefore, the He-like species begins to appear closer to the target because it is predominantly formed in the region that has a density higher than the critical density and which attains a lower expansion velocity. In particular at the peak of the laser pulse, the velocity of the innermost zone where the plasma is predominantly composed of He-like ions decreases a factor of 2.3 for laser intensities increasing from 5×10^{12} to 5×10^{13} W/cm^2. This effect explains why the He-like absorption begins closer to the target, and why the extension of the lesser charged ion absorption is smaller, i.e., the absorption region remains closer to the target in photograph 3(b) than in 3(a). The theoretical velocities are within a factor of 2 from the estimate made from the data because they are dependent on the theoretical intensity entered into the code. But the trend of lower velocities for the higher intensities is unmistakable in both the experimental data and the simulations. It should be noticed that this inverse relationship is contrary to the usual scalings of measured and calculated coronal velocities with laser intensity because it concerns the overdense plasma which has expanded out after the laser pulse.

The slope of the curve does not vary with laser intensity or different flux limiters ranging from values of 0.12 to 0.24, however the slope may be affected by two-dimensional effects or radiative heating. The effect of bi-dimensional expansion has been explored by using a 1.5-dimension version of FILM. It is a pseudo-one-dimensional calculation that accounts for the lateral, i.e., perpendicular to the laser axis, hydrodynamic expansion of the plasma by analogy with an analytic self-similar expansion of a plasma that has a Gaussian spatial distribution of density and a constant temperature [14]. These simulations predict that for a given laser intensity the average ionic charge far from the target is very similar to that given by the one-dimensional calculation; however, the ionization of the Be-like to Li-like species occurs farther from the surface and the maximum displacement is ~10 μm. Since the atomic model in both FILM simulations is the same, the change in the slope of the gradient is due to the enhanced hydrodynamic cooling occurring in the 1.5-dimension simulation.

The changes in the slope of the thermal gradient due to radiative heating were explored by the code XRAD [15]. The hydrodynamics in this code are in principle similar to FILM, however the radiative transfer equation is included and resolved using a multigroup, multiangle approach. Comparisons of the simulations with and without radiative transfer show that radiative heating does tend to smooth out the gradient and can shift the absolute positions by up to 10 μm farther away from the target for the higher ionized species.

Analysis of the series of shots confirms predictions of the simulations. The two shots shown in Fig. 5 are representative of the entire series of shots. As the laser flux increases, the slope of the Z gradient tends to becomes sharper and is located closer to the zero position of the target surface. Simulations taking into account two-dimensional expansion or radiative heating show that these effects may cause a softening of the slope.

V. FURTHER ANALYSIS OF THE SPECTRA

In addition to the average Z, the spectra can be further analyzed to extract the traditional plasma parameters temperature and density. However, this application of the $K\alpha$ diagnostic is to plasmas of *subcritical* density and requires a non-LTE calculation of the ionization balance. The mechanics of generating a synthetic absorption spectrum is now coupled to a non-LTE calculation of the ionization instead of an experimental fit or a LTE calculation.

The ionization is computed using a hydrogenic steady-state non-LTE model in which the relevant collisional and radiative rates are calculated and then the populations are found by inverting the rate matrix. The popula-

tion of each generalized hydrogenic ground state is then distributed by the Boltzmann factor among the manifold of ground states calculated by a detailed atomic model for that particular ion. Since the maximum difference between the detailed ground-state energy levels of any particular ion is only 12 eV on average, this assumption of LTE between the intra-ground-state configurations of each ion should still be valid at densities as low as 10^{18} cm^{-3} [16]. According to hydrodynamic codes, the use of a steady-state model is applicable because the calculations indicate that the stationary and nonstationary average charge of the plasma are virtually identical for a region extending more than 200 μm from the target at the time probed.

With a model for the ionization balance, the spectrum can now be analyzed to yield either the temperature or the density. Since an independent measurement of the electron temperature or density was not available during these experiments, we use simulations to provide one of these parameters. Given one parameter, the other is inferred by varying it until the synthetic spectrum matches the experimental spectrum. This type of plasma is expected to have an ionization falling between LTE and coronal equilibrium limits depending on its density. Close to the target, the near-LTE ionization balance is more strongly temperature dependent than density dependent; a factor-of-10 change in density is necessary to affect the same ionization balance change caused by a 5-eV change in temperature. Far from the target, the coronal ionization balance is density independent. The ionization becomes less and less dependent on density for steady-state calculations. Hence for further discussions, we choose to input the density and infer the temperature.

Although the quality and intensity of the backlight during these experiments was insufficient to permit a precise enough quantification of the absolute populations from the experimental spectra, we can estimate a limit on the He-like ionic density to see if this is reasonable. Here we choose a point at which the temperature gradient is not large. For a spectrum taken at 100 μm, the synthetic spectrum matches the experimental spectrum for an electron temperature of 70 eV and an electron density of 1.5×10^{20} cm^{-3}. For a 200 μm length of plasma probed, the maximum limit on the absolute ionic population in this ground state is 7×10^{19} cm^{-3} and is consistent with the measurements of the absolute population by the resonance line method of O'Neill *et al.* [17]. This correlation gives added confidence in the density gradient calculated by the codes.

In laser-produced plasmas, the temperature typically rises quickly as a function of distance from the target surface and then levels out in the corona. Comparisons to the modeling indicate that in the ionization front it is never possible to account for the many species using a one-temperature, one-density model. Instead of introducing a temperature gradient into the calculations, we choose to use the average ionic charge to determine the average temperature in this region. This leads to a practical modification of the criteria for fitting the theoretical and experimental spectra: the temperature is varied until the average ionic charge matches the experimental ionic charge. For comparison to the hydrodynamics codes, this should be a sufficient criteria in the dense regime. However, after the average Z has finished its sharp rise, the spectrum can be reproduced by a single temperature and density. For instance, in the low-energy shot shown in Fig. 4(a), this occurs from 100 μm onward. For distances greater than this from the target, the temperature is inferred more accurately by using the criteria that the theoretical spectrum matches the experimental one.

An important question to address here is whether lateral temperature and density measurements could affect the inference of a meaningful temperature. To investigate the hydrodynamic effect of a true two-dimensional expansion on the plasma temperature and density gradients, a two-dimensional code was used [18]. This code has a rudimentary description of the atomic physics occurring in the plasma and, although not suitable for the detailed plasma ionization characterization, it is appropriate for predictions of the lateral gradients. At these late probe times, the lateral temperature gradient is smoothed out due to efficient electron conduction in the corona. The density gradient from these same simulations also shows a smoothing out, though not as marked. The bulk of the remaining density gradient is found to be in the laser-produced plastic plasma that surrounds and tamps the lateral expansion of the aluminum microdot plasma. Since the plasma chord probed by the backlight photons changes negligibly, <2 μm, in distance from the target, the density can be assumed to be constant along the line of sight in this study. Hence, the interpretation of these data is not hampered by these plasma gradients.

In Fig. 6 we show the temperatures as a function of position which are calculated by the simulations along with those inferred from the data. The 1- and 1.5-dimension simulations for a laser intensity of 5×10^{12} W/cm^2 are shown by the solid and dotted lines, respectively. For each of the simulations, two temperature curves are shown—one corresponding to the beginning of the 500-ps backlight and one at the end. The temperature range bracketed between each pair of curves indicates the magnitude of the cooling that takes place during the time frame of the backlight. The temperature inferred from

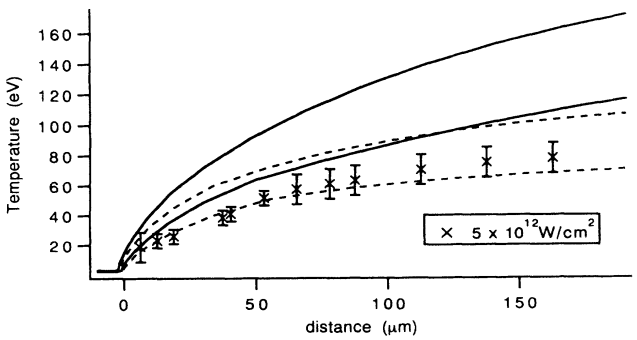

FIG. 6. Temperatures calculated by the hydrodynamics codes and temperatures deduced from the absorption data. The solid lines correspond to the minimum and maximum temperatures during the 500-ps probe time for the 1-D case and the dotted lines to the 1.5-D case.

the data is bracketed by using the densities calculated by both the 1- and 1.5-dimension simulations for each point.

For distances less than 100 μm, the temperature has a behavior very similar to the average Z. The simulations calculate that the electron density is greater than 3×10^{20} cm^{-3} and in this high-density regime the $K\alpha$ absorption structures vary more importantly with temperature because the existence of the relaxing thermal front causes a change in temperature that has a larger impact on the ionization than the change in density.

At distances greater than 100 μm, the temperature calculated by the codes and inferred from the experiments all tend to reach a plateau, however the final values are quite different even though the average Z values are nearly constant and equal. In essence in the corona, the temperature varies very little and the average ionic charge is now affected as much by the density as by the temperature. In these simulations the $\langle Z \rangle$ remains constant because of the compensating effects of the falling temperature and density in the corona. The 1.5-D case shows the effect of the enhanced cooling of the plasma due to its expansion which is more and more pronounced as the distance farther from the surface is probed.

The character of the inferred temperature agrees with the simulations, however a resolution better than 10 μm is necessary near the target surface to resolve and differentiate between the temperature gradients. In general, the inferred temperature compares most favorably to the 1.5-dimension simulation indicating that the expansion of the dot is not planar, which is expected since the laser focal spot was less than twice the diameter of the microdot.

VI. CONCLUSIONS

In this paper we demonstrate the potential of $K\alpha$ absorption to diagnose subcritical density plasmas at late times after the laser pulse. The position and extension of the ionic species in space are measured at a time 1.4 ns after the creation of the plasma. The advantage in probing at late times is that the deeply heated plasma has time to expand out and one can measure the evolution of the ionization front after the pulse. For a laser intensity of 5×10^{12} W/cm^2, the peak absorption of the He-like species is located approximately 100 μm from the target surface and extends into the low-density plasma. The appearance of the lesser ionized species, F-like to Li-like close to the target, is due to the evolution of the ionization front at late time.

These absorption experiments relate the absolute position of the ionic species to the laser intensity on target. Hydrodynamic simulations indicate that the gradient of the average Z becomes steeper and is located closer to the surface of the irradiated target as the laser energy is increased. The experimental results confirm this trend.

This study focuses on the average ionization and presents the validity of the measurement itself. Near the surface of the target, the collisional rates are strong enough to establish a steady-state equilibrium. In this case, the temperature very closely follows the average Z and if coupled with a density measurement, the ionic charge determined by absorption spectroscopy could serve as a benchmark of the hydrodynamics codes that simulate the expanding plasma. This means that the nonstationary cooling of the ionization front which is sensitive to the atomic physics in the hydrodynamic codes could be explored in more detail. Other applications could include the investigation of the effects of radiative heating or hydrodynamic cooling.

$K\alpha$ absorption spectroscopy resolved in space can be a powerful diagnostic to characterize plasmas for photopumping or x-ray laser studies. Future experiments can exploit this diagnostic in conjunction with an independent temperature or density measurement to measure the density or temperature of the plasma. Hence warm plasmas, whether dense or underdense, can be probed by this $K\alpha$ absorption technique.

ACKNOWLEDGMENTS

We would like to thank the LULI laser staff for this help, in particular A. M. Tournade and J. P. Zou for their expertise in keeping the laser up and running, and R. Konig for his help in the darkroom. Also, J. Virmont and N. Grandjouan have been helpful in the discussions concerning the simulations.

[1] A. Hauer, R. W. Cowan, B. Yaakobi, O. Barnouin, and R. Epstein, Phys. Rev. A **34**, 411 (1986).

[2] C. Chenais-Popovics, C. Fievet, J. P. Geindre, J. C. Gauthier, E. Luc-Koenig, J. F. Wyart, H. Pépin, and M. Chaker, Phys. Rev. A **40**, 3194 (1989).

[3] S. J. Davidson, D. Neely, C. L. S. Lewis, and D. O'Neill, Annual Report 1990, RAL-90-026, p. 13 (unpublished).

[4] R. Epstein, Phys. Rev. A **43**, 961 (1991).

[5] T. S. Perry, S. J. Davidson, F. J. D. Serduke, D. R. Bach, C. C. Smith, J. M. Foster, R. J. Doyas, R. A. Ward, C. A. Iglesias, R. J. Rogers, J. Abdallah, Jr., R. E. Stewart, J. D. Kilkenny, and R. W. Lee, Phys. Rev. Lett. **67**, 3784 (1991).

[6] C. A. Back, P. Renaudin, C. Chenais-Popovics, and J. C. Gauthier, Laser Part. Beams (to be published).

[7] C. Danson R. Bann, D. Pepler, I. Ross, J. Exley, D. Hardie, and S. Sails, Annual Report 1991, RAL-91-025, p. 62 (unpublished).

[8] C. L. S. Lewis and J. McGlinchey, Opt. Commun. **53**, 179 (1985).

[9] A. Zigler, M. Givon, E. Yarkoni, M. Kishinevsky, E. Goldberg, B. Arad, and M. Klapisch, Phys. Rev. A **35**, 280 (1987).

[10] J. Balmer, C. L. S. Lewis, R. E. Corbett, E. Robertson, S. Saadat, D. O'Neill, J. D. Kilkenny, C. A. Back, and R. W. Lee, Phys. Rev. A **40**, 330 (1989).

[11] J. P. Geindre, C. Chenais-Popovics, P. Audebert, C. A. Back, J. C. Gauthier, H. Pepin, and M. Chaker, Phys. Rev. A **43**, 3202 (1991).

[12] J. F. Lucianai, P. Mora, and J. Virmont, Phys. Rev. Lett. **51**, 1664 (1983); J. F. Luciani and P. Mora, Phys. Lett. **A116**, 237 (1986).

[13] L. Spitzer, *Physics of Fully Ionized Gases* (Interscience, New York, 1965).
[14] J. Virmont, N. Grandjouan, A. Klisnick, Internal Report, LULI Rapport Scientifique 1990, p. 21 (unpublished).
[15] J. C. Gauthier and J. P. Geindre, Laboratoire PMI, Ecole Polytechnique Report No. PMI 1974 (1988), available upon request (unpublished).
[16] H. R. Griem, *Plasma Spectroscopy* (McGraw-Hill, New York, 1964).
[17] D. M. O'Neill, C. L. S. Lewis, D. Neely, S. J. Davidson, S. J. Rose, and R. W. Lee, Phys. Rev. A **44**, 2641 (1991).
[18] N. Grandjouan (private communication).

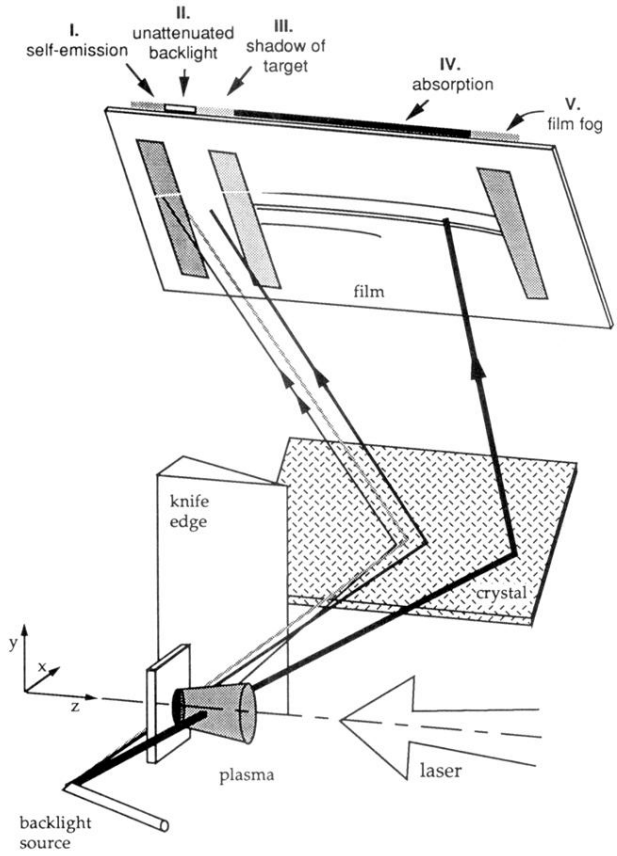

FIG. 2. Schematic diagram of the experimental arrangement and the film regions. The line with the double arrow head shows the path of the photons due to self-emission onto the region which is shielded from the backlight by the knife edge. The dark solid line shows the backlight photons that probe the plasma. The grey line shows the projection of the knife edge onto the film by the backlight.

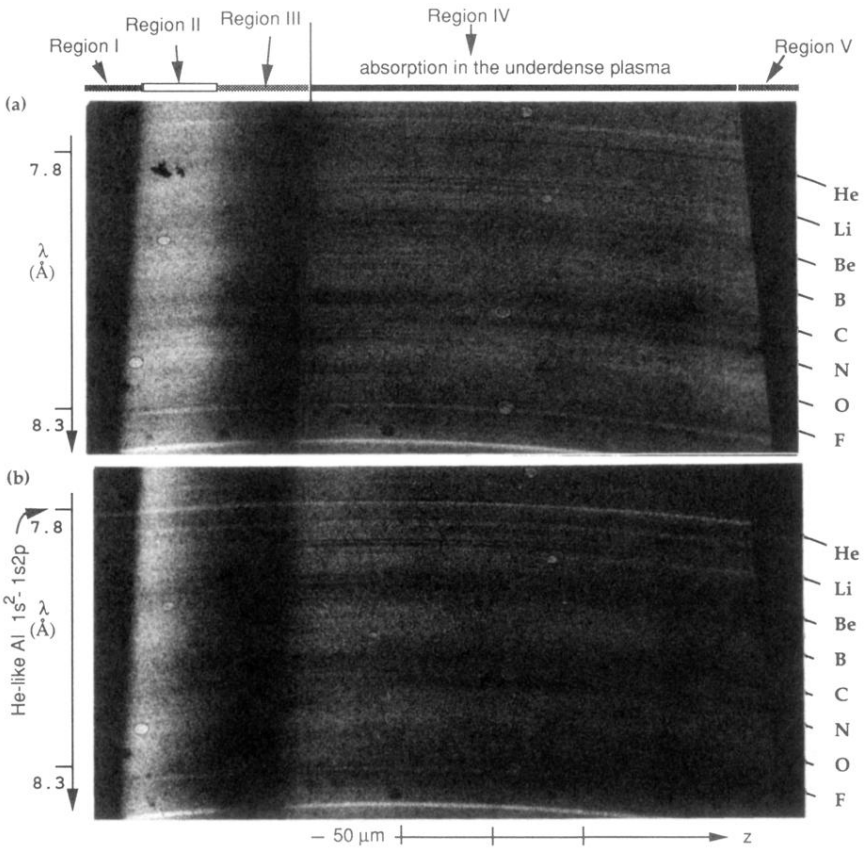

FIG. 3. Two photographs of the data. The film regions are identified in the upper margin. The dark lines correspond to absorption and are labeled by their isoelectronic sequence, i.e., Al XII=He. The absorption for a plasma created by a 0.53-μm laser: (a) laser energy 3 J, no He-like resonance line emission is visible; (b) laser energy 5 J, the He-like Al, $1\,^1S_0-2\,^1P_1$, resonance line in emission is indicated in region I.